Appl. Phys. B 56, 71–78 (1993)

Applied Physics B Photophysics and Laser Chemistry

Chemically Pumped $O_2(a–X)$ Laser

M. Endo, K. Kodama, Y. Handa, and T. Uchiyama

Department of Electrical Engineering, Faculty of Science and Technology, Keio University, 3-14-1, Hiyoshi, Kohoku-ku, Yokohama, 223, Japan (Tel.: +81-45/563-1141 ext. 3338, Fax: +81-45/563-2773)

Received 1 October 1992/Accepted 29 October 1992

Abstract. A theoretical and experimental study was conducted aimed at achieving laser oscillation in the $(a–X)$ electronic transition of oxygen molecules. Although this transition is highly forbidden by rigorous selection rules, it may nevertheless concede stimulated emission, if the population inversion is high enough. The idea is based on a recently developed apparatus, namely, a porous pipe type high-pressure chemical singlet oxygen generator. A numerical model which describes the characteristics of this generator was developed to estimate the population inversion and small-signal gain achievable in a laser cavity using this source. The calculations showed that the small-signal gain ought to be sufficient to achieve laser oscillation. Preliminary experiments were conducted, but lasing was not yet observed. It is shown that the scattering losses caused by water droplet aerosols are mainly responsible for preventing our system from laser oscillation.

PACS: 42.55.Ks, 42.55.Lt

A theoretical and experimental study of a high-pressure chemical singlet oxygen generator was conducted aimed at achieving laser oscillation in the $(a–X)$ electronic transition of oxygen molecules. An oxygen molecule excited to the first excited level is in a $^1\Delta_g$ electronic state, and has an energy of 0.98 eV above the $^3\Sigma_g^-$ ground state. One of the interesting properties of $O_2(a^1\Delta_g)$ is that the radiative transition to the ground state has an extremely long lifetime of 65 min [1]. This is due to the fact the $^1\Delta_g$–$^3\Sigma_g^-$ transition is doubly forbidden by the rigorous selection rules for dipole radiation and singlet-triplet intercombination. Furthermore, the $^1\Delta_g$–$^3\Sigma_g^-$ system violates the selection rule $\Delta\Lambda = 0, \pm 1$, for electric and magnetic dipole radiation. Although stimulated emission at this transition appears thus to be almost impossible, it has nevertheless the potential to be a new high-energy laser since the stored energy density in the metastable excited states can be higher by a few orders of magnitude than in presently known laser media. There are only a few reports dealing with this subject experimentally or theoretically. Scully et al. [2] pointed out theoretically that the energy stored in metastable excited states of diatomic molecules such as N_2 and O_2 can be extracted efficiently by means of strong π-pulse radiation. Kerber et al. [3] constructed an $O_2(a–X)$ laser system and made some experiments. They utilized an ozone generator and flashlamps to generate $O_2(a^1\Delta_g)$ at high pressure photolytically. They reported that a laser-like end light, which was different from the side light in waveform, was observed. However, they could not prove that it was an oscillation. Since then, according to our knowledge, there are no reports about the experimental study of this subject.

We developed a porous-pipe chemical singlet oxygen generator (SOG) in 1986 [4] and found that it was suitable as an $O_2(a^1\Delta_g)$ source of the $O_2(a–X)$ laser. This SOG generates $O_2(a^1\Delta_g)$, utilizing a horizontally placed ceramic porous pipe which is rotated by a motor and wetted uniformly by basic hydrogen peroxide. Singlet oxygen is generated at the surface of the pipe when chlorine gas is fed into it. The overall reaction is described as follows:

$$H_2O_2 + 2\,MOH + Cl_2 \rightarrow 2\,H_2O + 2\,MCl + O_2(a^1\Delta_g)\,, \quad (1)$$

where M denotes an alkali metal such as sodium or potassium. This SOG had a higher yield than conventional bubbler-type SOGs, such that it contributed to the successful operation of a chemically pumped oxygen-iodine laser without a water vapor trap [5]. We found that this type of SOG could be a new high-pressure singlet oxygen source, so we have been studying the development of a high-pressure SOG, keeping the $O_2(a–X)$ laser in mind.

1 Theory

1.1 $O_2(a^1\Delta_g)$–$O_2(X^3\Sigma_g^-)$ *Transition*

Since the $O_2(a^1\Delta_g)$–$O_2(X^3\Sigma_g^-)$ transition is electric dipole forbidden, it can appear only as a magnetic dipole transition or as an electric quadrupole transition. Practically, the latter can be neglected for our purposes. This transi-

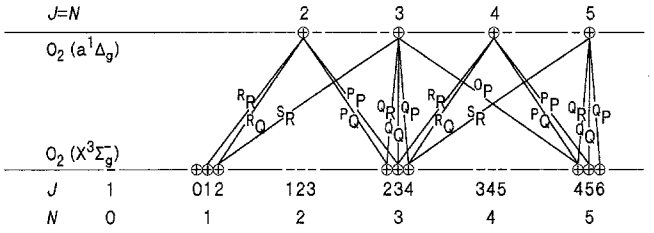

Fig. 1. Origin of the branches in a $^1\Delta_g$–$^3\Sigma_g^-$ transition [9]. The levels that occur for the O_2 molecule are circled

tion is restricted by one of the selection rules governing magnetic dipole transitions, which is $\Delta J = 0, \pm 1$, J being the total angular momentum. The transition is also governed by the selection rules for singlet–triplet transition, which is $\Delta N = 0, \pm 1, \pm 2$, where N is the total angular momentum apart from electron spin. The upper state $^1\Delta_g$ always takes $J = N$ as a singlet state while the lower level $^3\Sigma_g^-$ can take one of the triply degenerated states, $J = N$, $J = N + 1$, or $J = N - 1$. Moreover, the ground-state oxygen can occupy only odd rotational quantum numbers because the nuclear spin of $O_2(X^3\Sigma_g^-)$ molecule is zero [7]. The $^1\Delta_g$ state has no level with $J = 0$ or $J = 1$. The transitions possible on the basis of the above mentioned rules are indicated in the schematic diagram (Fig. 1).

1.2 Rotational Level Distribution

We do not consider the vibrational structure of the transition because reaction (1) selectively produces $O_2(a^1\Delta_g)$ in the $v = 0$ level, and the (0–1) band intensity is one hundredth of the (0–0) band intensity [8]. On the other hand, the rotational level distribution is important in order to estimate the relative intensity of the various transitions. We assume a Boltzmann function for the rotational distribution because the level spacing of each rotational level is much less than the value of kT at room temperature. We assume that the Boltzmann distribution is not distorted by lasing because all processes including stimulated emission are much slower than the reequilibration of the rotational levels under the conditions we are considering. It should be noted that this assumption is not valid for a short pulse amplifier.

The rotational level distribution is calculated by the rotational term values of each level. For $O_2(a^1\Delta_g)$, it is simply described by the rigid rotor approximation,

$$F'(J) = BJ(J+1)\,, \tag{2}$$

where $B = 1.4178\,\mathrm{cm}^{-1}$ is the rotational constant [9], and J is the total angular momentum quantum number. However, the term values of $O_2(X^3\Sigma_g^-)$ molecules are rather complicated due to triplet degeneration, coupling of the spin to the internuclear axis, and coupling between the electron spin and the axis of rotation. This is expressed by

$$\begin{aligned} F_1''(J) &= J(J+1)B + (2\lambda - \gamma) \\ &\quad + (B - \lambda - \gamma/2) - [b - \lambda - \gamma/2)^2 \\ &\quad + 4J(J+1)\,(B - \gamma/2)^2]^{1/2}\,, \end{aligned} \tag{3a}$$

$$F_2''(J) = J(J+1)B + (2\lambda - \gamma)\,, \tag{3b}$$

and

$$\begin{aligned} F_3''(J) &= J(J+1)B + (2\lambda - \gamma) \\ &\quad + (B - \lambda - \gamma/2) + [(b - \lambda - \gamma/2)^2 \\ &\quad + 4J(J+1)\,(B - \gamma/2)^2]^{1/2} \end{aligned} \tag{3c}$$

where $B = 1.43777\,\mathrm{cm}^{-1}$, $\lambda = 1.984\,\mathrm{cm}^{-1}$ and $\gamma = -0.0084\,\mathrm{cm}^{-1}$ are the inertial and coupling constants [10]. In these term values, F_1'', F_2'' and F_3'' correspond to $(N = J - 1)$, $(N = J)$ and $(N = J + 1)$, respectively. The relative term values of these three levels in the same N are $F_1'' \doteqdot F_3''$, and F_2'' is approximately $2\,\mathrm{cm}^{-1}$ higher than F_1'' and F_3''. Note that the N number of $O_2(X^3\Sigma_g^-)$ must be odd due to zero nuclear spin.

1.3 Estimation of the Einstein A-Coefficient of Each Transition

The transition probability for each line can be calculated theoretically by employing the general law of the rotational distribution on the $^1\Delta_g$–$^3\Sigma_g^-$ transition [11, 12]. Generally, the relative line intensity of spontaneous emission from an upper level (N') to a lower level (N'', J'') is expressed in terms of the Hönl-London factor and the rotational distribution function,

$$I(N' \to N'', J'') \propto i(J'') \exp[-F'(J')hc/kT]\,. \tag{4}$$

Here,

$I(N' \to N'', J'')$:	Spontaneous emission intensity,
$i(J'')$:	Corresponding Hönl-London factor,
$F'(J')$:	Rotational term value of the upper level $[\mathrm{cm}^{-1}]$,
h:	Planck's constant,
c:	Velocity of light [cm/s],
k:	Boltzmann's constant,
T:	Absolute temperature.

The Einstein A-coefficient of a particular transition is proportional to the spontaneous emission intensity divided by the number density of the upper state. Assuming a Boltzmann distribution, this works out to:

$$A_{21}(N' \to N'', J'') = Ki(J'')/(2N' + 1)\,, \tag{5}$$

where K is an undetermined constant. Since the observed spontaneous emission probability is the sum of the transitions from all rotational levels, it is expressed by the following summation in terms of fractional population distributions and spontaneous emission probability of each transition,

$$\begin{aligned} A_{21} &= \sum_{N', N'', J''} [p(N')A_{21}(N' \to N'', J'')] \\ &= \frac{K}{Q(^1\Delta)} \sum_{N', N'', J''} i(J'') \exp[-F'(J')hc/kT]\,, \end{aligned} \tag{6}$$

where $p(N')$ is the fractional population of $O_2(a^1\Delta_g)$, distributed in (N') rotational level, A_{21} is the observed Einstein A-coefficient, and $Q(^1\Delta)$ is the partition function of $O_2(a^1\Delta_g)$. The A-coefficient of a particular transition is obtained by solving (6) for K and substituting it into (5). This

leads to

$$A_{21}(N' \to N'', J'') = A_{21} \frac{i(J'')Q(^1\Delta)}{(2N'+1)\sum_{N',N'',J''} i(J'')\exp[-F'(J)hc/kT]}. \quad (7)$$

In this way, the A-coefficient that we used in our model calculations is given as a function of N', N'' and J''.

The stimulated emission cross section of each transition is expressed as

$$\sigma(N' \to N'', J'') = \lambda^2 A_{21}(N' \to N'', J'')g(\nu_o)/8\pi\,, \quad (8)$$

where $g(\nu_0)$ is the value of the line-shape function at line center. The Voigt profile was used for our calculations because the operating pressure of our SOG was of the order of 10 kPa. The pressure broadening coefficient is 24 kHz/Pa [1]. The small signal gain is obtained in terms of a stimulated emission cross section and a population inversion density as

$$\alpha(N' \to N'', J'') = \sigma(N' \to N'', J'')\Delta N(N' \to N'', J'')\,, \quad (9)$$

where

$$\Delta N(N' \to N'', J'') = [O_2(a^1\Delta_g)](N') - \frac{2N''+1}{2N''+1}[O_2(X^3\Sigma_g^-)](N'', J'')\,, \quad (10)$$

where $[O_2(a^1\Delta_g)](N')$ is the number density of the $O_2(a^1\Delta_g)$ populating the (N') rotational level and the number density of $[O_2(X^3\Sigma_g^-)](N'', J'')$ is defined in the same way. Table 1 shows the spontaneous emission probability of each line for rotational levels below $N = 15$, and Table 2 shows the corresponding stimulated emission cross section at 4 kPa.

2 Theoretical Study

In this section, the theoretical study of a $O_2(a\text{–}X)$ laser is discussed. A numerical model describing the property of our high-pressure pulsed SOG is formulated and a detailed $O_2(a^1\Delta_g)$–$O_2(X^3\Sigma_g^-)$ transition, including the rotational structure, is incorporated into this model.

2.1 Formulation of a Numerical Model

First of all, a physical model is defined. The model of the chemically-pumped oxygen-laser system is depicted in Fig. 2. The model consists of a laser cavity, a chlorine tank, and a Cl_2–O_2 converter connecting the cavity and the Cl_2 tank. For simplicity, we employed a point-source model for the rate equations in the laser cavity. This approximation is valid since the aperture of the laser cavity is small compared to the product of the characteristic time of the fastest chemical reaction and the gas velocity.

The operation of the system is described in order to follow the performance of our SOG [6]. The pressure of the

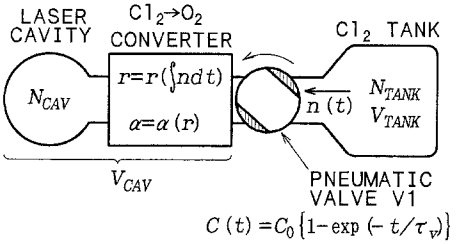

Fig. 2. Schematic drawing of the numerical calculation model. N denotes the number density and V denotes the volume of each component

Table 1. Einstein coefficients A_{21} below $N = 15$ [$10^{-4}s^{-1}$]

N	$J = N-1$			$J = N$			$J = N+1$		
	$^OP(J)$	$^PQ(J)$	$^QR(J)$	$^PP(J)$	$^QQ(J)$	$^RR(J)$	$^QP(J)$	$^RQ(J)$	$^SR(J)$
1	–	–	–	–	–	1.538	–	0.513	0.732
3	–	0.342	0.488	0.171	1.068	1.068	0.153	0.641	0.544
5	0.122	0.513	0.435	0.342	1.196	0.920	0.209	0.657	0.473
7	0.179	0.563	0.406	0.423	1.236	0.848	0.237	0.660	0.436
9	0.211	0.586	0.388	0.469	1.253	0.806	0.254	0.659	0.414
11	0.231	0.599	0.376	0.499	1.262	0.778	0.266	0.658	0.399
13	0.245	0.607	0.368	0.521	1.268	0.758	0.274	0.657	0.388
15	0.255	0.613	0.362	0.536	1.271	0.743	0.280	0.655	0.380

Table 2. Stimulated emission cross section below $N = 15$ [$10^{-22}cm^2$] (Pressure = 4 kPa, temperature = 293 K, pressure broadening coefficient = 24 kHz/Pa)

N	$J = N-1$			$J = N$			$J = N+1$		
	$^OP(J)$	$^PQ(J)$	$^QR(J)$	$^PP(J)$	$^QQ(J)$	$^RR(J)$	$^QP(J)$	$^RQ(J)$	$^SR(J)$
1	–	–	–	–	–	1.529	–	0.510	0.728
3	–	0.340	0.485	0.170	1.062	1.062	0.152	0.637	0.541
5	0.121	0.510	0.432	0.340	1.189	0.915	0.208	0.653	0.470
7	0.178	0.560	0.403	0.420	1.229	0.843	0.236	0.656	0.434
9	0.210	0.583	0.386	0.466	1.246	0.801	0.253	0.655	0.412
11	0.230	0.596	0.374	0.496	1.255	0.773	0.264	0.654	0.396
13	0.244	0.604	0.366	0.518	1.260	0.753	0.272	0.653	0.386
15	0.254	0.609	0.360	0.533	1.264	0.738	0.278	0.652	0.377

cavity is initially 110 Pa, and the only component is water vapor. The Cl_2 tank contains pure chlorine gas at a pressure of several of atmospheres. Valve V1 starts to open at $t = 0$, and it takes a few tens of milliseconds to open it completely. Therefore, the conductance of the channel between the Cl_2 tank and the laser cavity is time dependent. We simulated it by a simple exponential function:

$$C = C_0[1 - \exp(-t/\tau_V)], \tag{11}$$

where C_0 is the final conductance of the channel [$cm^3\,s^{-1}$], and τ_V is the opening time of V1, defined to be 50 ms by the analysis of the experimental results. When the valve is opened, Cl_2 gas is injected into the Cl_2–O_2 converter. This converter simulates the porous-pipe type SOG. The conversion efficiency of the converter is defined as a function of the total number of injected Cl_2 molecules up until that moment. The yield of $O_2(a^1\Delta_g)$ of the generated oxygen, that is to say the transient ratio of $O_2(a^1\Delta_g)$ to oxygen being discharged from the converter, is defined as a function of the conversion efficiency. The conversion efficiency, in a first-order approximation, can be written as

$$r(t) = \begin{cases} 1 - \int_0^t ndt/N_0 & \left(\int_0^t ndt \leqq N_0\right) \\ 0 & \left(\int_0^t ndt > N_0\right), \end{cases} \tag{12}$$

in accordance with the observed results [6]. Here, r is the conversion efficiency, $n(t)$ is the chlorine injection rate [molecules/s] and N_0 is a constant obtained by an analysis of the experimental results. The $O_2(a^1\Delta_g)/O_2$ ratio is not defined in this step. The injection rate of Cl_2 is a function of the pressure difference between the tank and the cavity, and the time-dependent conductance C, written as

$$n(t) = C(N_{TANK} - N_{CAV}), \tag{13}$$

where N_{TANK} and N_{CAV} is the total number density of molecules in the Cl_2 tank and the laser cavity, respectively.

The only variable in this model which cannot be measured experimentally is the transient ratio of $O_2(a^1\Delta_g)$ to oxygen being discharged. We call this value "transient yield". The derivative of the $O_2(a^1\Delta_g)$ pressure with respect to t does not give the transient yield because $O_2(a^1\Delta_g)$ is deactivated by various reactions. It is clear that the yield of $O_2(a^1\Delta_g)$ strongly depends on the reaction efficiency, since oxygen molecules are generated by the penetration of Cl_2 molecules into the solution, conversion to oxygen, and subsequent diffusive escape out of the solution. If the reaction efficiency is high, the average depth of oxygen generation in the gas-liquid interface becomes shorter, and this makes the deactivation length smaller [13]. There are some papers dealing theoretically with the relation between the depletion of the HO_2^- ion and $O_2(a^1\Delta_g)$ yield [14, 15]. However, these theories assume that the HO_2^- ion concentration is independent of the distance from the gas-liquid interface. This was not the case with our system, because the HO_2^- ion density is not equilibrated due to the extremely high concentration of chlorine. Instead, we defined the transient yield empirically as

$$\alpha(r) = \alpha_0 r^x, \tag{14}$$

where α_0 is the observed initial yield of the SOG and x is an undetermined constant. We thought that this function could be fit to the actual relation to some extent, because (14) could trace an arbitrary path between $(1, \alpha_0)$ and $(0, 0)$. We determined the parameter x by fitting the calculated results to those observed.

Finally, a set of rate equations governing the density of the species are written as follows:

$$d[O_2(b^1\Sigma_g^+)]/dt = \chi^{pro}\{O_2(b^1\Sigma_g^+)\} - \chi^{dis}\{O_2(b^1\Sigma_g^+)\}, \tag{15a}$$

$$d[O_2(a^1\Delta_g)]/dt = \chi^{pro}\{O_2(a^1\Delta_g)\} - \chi^{dis}\{O_2(a^1\Delta_g)\} + \alpha rn/V_{CAV} - \chi^{ph}, \tag{15b}$$

$$d[O_2(X^3\Sigma_g^-)]/dt = \chi^{pro}\{O_2(X^3\Sigma_g^-)\} - \chi^{dis}\{O_2(X^3\Sigma_g^-)\} + (1-\alpha)rn/V_{CAV} + \chi^{ph}, \tag{15c}$$

$$d[Cl_2]/dt = (1-r)n/V_{CAV}, \tag{15d}$$

$$d[H_2O]/dt = 0, \tag{15e}$$

$$dN_{TANK}/dt = -n/V_{TANK}, \tag{15f}$$

$$dn_P(N' \to N'', J'')/dt = \{\sigma(N' \to N'', J'') \times \Delta N(N' \to N'', J'') - L\} \times n_P(N' \to N'', J'')c + A_{21}(N' \to N'', J'')\,p(N')[O_2(a^1\Delta_g)]S/(4\pi l^2), \tag{15g}$$

$$\chi^{ph} = \sum_{N',N'',J''} dn_P(N' \to N'', J'')/dt + Ln_P(N' \to N'', J'')c. \tag{15h}$$

Here, $(N' \to N'', J'')$ means a particular rotational line, $S/4\pi l^2$ denotes the solid angle of the laser cavity and L is the loss of the cavity [cm^{-1}]. χ^{pro} and χ^{dis} represent the production and the dissipation reactions. For example,

$$\chi^{pro}\{O_2(a^1\Delta_g)\} = [O_2(b^1\Sigma_g^+)]\{k_2[H_2O] + k_3[O_2(X^3\Sigma_g^-)] + k_6[Cl_2]\}, \tag{15i}$$

$$\chi^{dis}\{O_2(a^1\Delta_g)\} = [O_2(a^1\Delta_g)]\{2k_1[O_2(a^1\Delta_g)] + k_4[O_2(X^3\Sigma_g^-)] + k_5[H_2O] + k_7[Cl_2]\}. \tag{15j}$$

The reactions considered and the pertinent rate constants are listed in Table 3.

We neglected the dimol radiation of oxygen,

$$2\,O_2(a^1\Delta_g) \to k_D\,2\,O_2(X^3\Sigma_g^-) + h\nu\ (634\,nm) \tag{16}$$

because the rate constant k_D [17] is 6 orders of magnitudes lower than the energy pooling reaction constant k_1, and no pressure-induced effects were observed in our experiments. For the stimulated emission process, we assumed fast reequilibration of the rotational distribution. No line overlapping is expected for the pressure range of our device since the pressure broadening is of the order of 0.01 cm^{-1}. The stimulated emission therefore occurs only at the strongest rotational transition.

Table 3. Reactions and rate constants of the oxygen laser[a]

	Reaction		Rate constant [$cm^3\ s^{-1}$]
1	$O_2(a^1\Delta_g) + O_2(a^1\Delta_g)$	$\rightarrow O_2(b^1\Sigma_g^+) + O_2(X^3\Sigma_g^-)$	$k_1 = 2.0 \times 10^{-17}$
2	$O_2(b^1\Sigma_g^+) + H_2O$	$\rightarrow O_2(a^1\Delta_g) + H_2O$	$k_2 = 6.7 \times 10^{-12}$
3	$O_2(b^1\Sigma_g^+) + O_2(X^3\Sigma_g^-)$	$\rightarrow O_2(a^1\Delta_g) + O_2(X^3\Sigma_g^-)$	$k_3 = 4.6 \times 10^{-17}$
4	$O_2(a^1\Delta_g) + O_2(X^3\Sigma_g^-)$	$\rightarrow O_2(X^3\Sigma_g^-) + O_2(X^3\Sigma_g^-)$	$k_4 = 1.7 \times 10^{-18}$
5	$O_2(a^1\Delta_g) + H_2O$	$\rightarrow O_2(X^3\Sigma_g^-) + H_2O$	$k_5 = 5.6 \times 10^{-18}$
6	$O_2(b^1\Sigma_g^+) + Cl_2$	$\rightarrow O_2(a^1\Delta_g) + Cl_2$	$k_6 = 4.5 \times 10^{-16}$
7	$O_2(a^1\Delta_g) + Cl_2$	$\rightarrow O_2(X^3\Sigma_g^-) + Cl_2$	$k_7 = 3.0 \times 10^{-18}$

[a] See [16]

2.2 *Results of Model Calculations*

2.2.1 Comparison of Model Calculations and Observed Results. First, the parameter x of (14) was determined by fitting the calculated $O_2(a^1\Delta_g)$ pressure to the observations by varying the parameter x. Figure 3 shows the observed $O_2(a^1\Delta_g)$ pressure as a function of time, and the calculated $O_2(a^1\Delta_g)$ pressure at the same boundary conditions with the parameter x being varied at 0, 1, 2, and 3. It can be seen that the calculation with $x = 2$ yields the best fit to the observed results. We thus assinged a value of 2 to the parameter x.

Figure 4 shows the observed $O_2(a^1\Delta_g)$ pressure and the observed total pressure as a function of time, as well as the calculated results for the same boundary conditions. It is apparent that the calculated results coincide well with the observed results. Therefore, it is possible to use this model to estimate the population inversion and the small-signal gain of the proposed $O_2(a\text{–}X)$ laser.

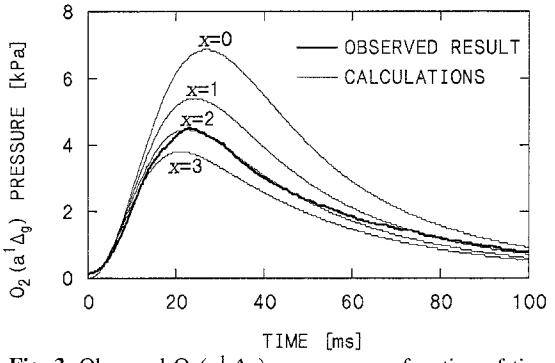

Fig. 3. Observed $O_2(a^1\Delta_g)$ pressure as a function of time and model calculations for the same boundary conditions with parameter x being varied

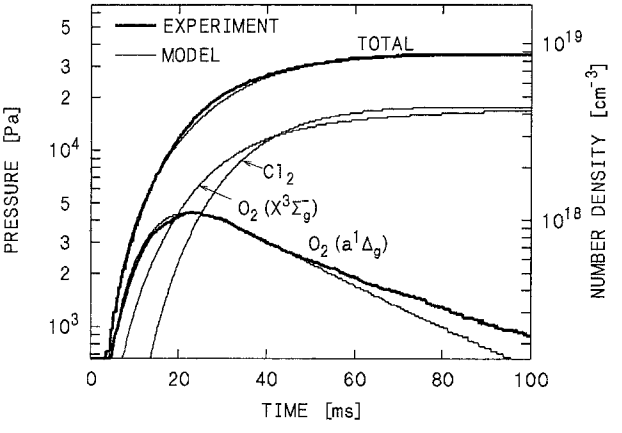

Fig. 4. Comparison of experimental results to the model calculation. Bold lines: Observed total pressure and $O_2(a^1\Delta_g)$ pressure as a function of time. Thin lines: Calculated total pressure, $O_2(a^1\Delta_g)$, $O_2(X^3\Sigma_g^-)$ and Cl_2 pressure as a function of time

2.2.2 Small-Signal Gain. We shall now discuss the feasibility of the $O_2(a^1\Delta_g)$ laser using this model. We calculated the peak small-signal gain as a function of two variables: the first is the ratio of the cavity volume to that of the Cl_2 tank, and the second is the initial yield of the SOG, α_0. Figure 5 shows the results. The open dot in this graph indicates the boundary conditions of our apparatus, which will be discussed later. The broken line represents the minimum cavity loss of our apparatus caused by the residual loss and transmittance of the resonator mirrors. In the series of calculations, the highest gain was always obtained at the ${}^QQ(9)$ transition ($9 \rightarrow 9, 9$).

The calculated result indicates that if there was no extra loss in the cavity, our system should lase. This graph also indicates that an improvement of the initial $O_2(a^1\Delta_g)$ yield from 0.7 to 0.8 boosts the small-signal gain by about 1.5 times. The investigation of the mechanism which deactivates $O_2(a^1\Delta_g)$ initially is also important.

2.2.3 Extractable Energy. Finally, the extractable energy of the $O_2(a^1\Delta_g)$ laser is estimated. Figure 6 shows the extractable energy per unit volume, and the chemical efficiency of an $O_2(a^1\Delta_g)$ laser as a function of the small-signal gain. The chemical efficiency is defined by the ratio

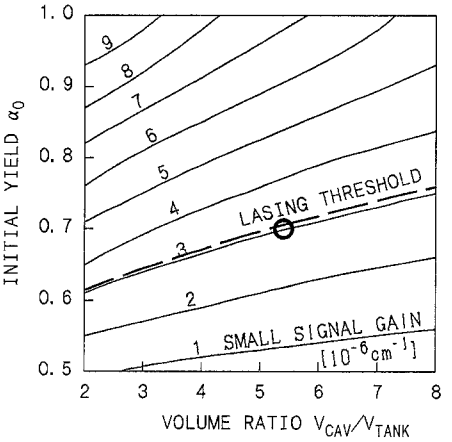

Fig. 5. Peak small-signal gain as a function of V_{CAV}/V_{TANK} and α_0. The open dot represents the real conditions of our apparatus. The broken line shows the lasing threshold

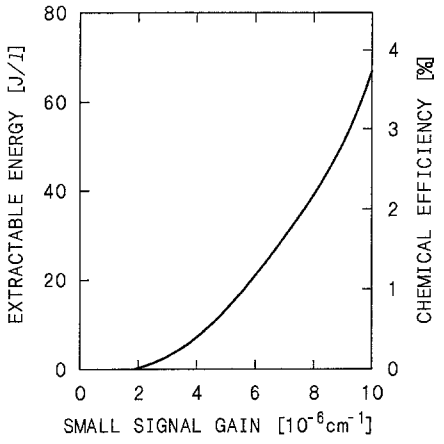

Fig. 6. Extractable energy and chemical efficiency as a function of small-signal gain

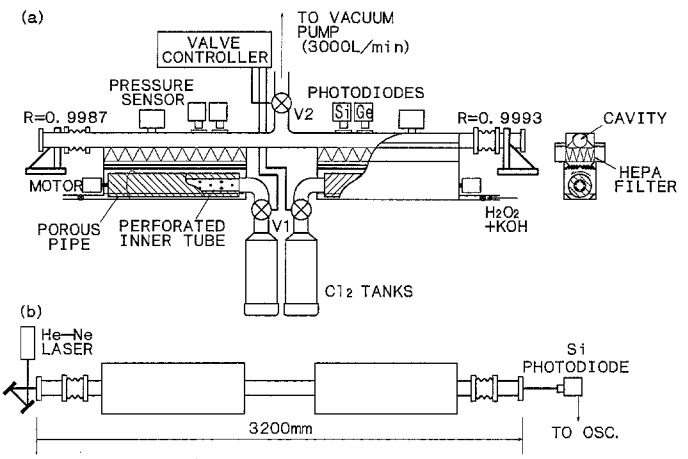

Fig. 7. a Schematic drawing of the apparatus. **b** Experimental setup of the cavity-loss measurement

of laser output energy to consumed chemical energy. The cavity loss, except for the mirror transmittance, is assumed to be $1.9 \times 10^{-6}\text{cm}^{-1}$, which is the nominal value of our resonator mirrors. In these calculations the volume ratio is fixed at 2.0 and the initial yield is varied. An extractable energy of 70 J/l can be expected when the small-signal gain reaches a value of $1 \times 10^{-5}\text{cm}^{-1}$. Under these conditions the chemical efficiency amounts to 3.7%.

3 Experiment

In accordance with these calculations, a laboratory device was developed and preliminary experiments were conducted. Figure 7a shows the schematic of the apparatus. Two SOGs are directly connected to a laser cavity of 3200 mm length. Internal mirrors having high reflectivity at 1.27 μm are mounted at the ends of the cavity. One mirror is curved ($R_C = 10\,\text{m}$) and has a reflectivity of 99.93%. The other mirror is flat and has a reflectivity of 99.87%. Throughout the resonator, the aperture is not smaller than 30 mm. The SOGs are identical to the one described in [6]. Each SOG comprises a solution tank, a chlorine tank, and a porous pipe on the surface of which $O_2(a^1\Delta_g)$ generation occurs. A newly developed air filter is employed for this application; it is located between the SOG and the laser cavity because the splashes produced in the SOG cause serious scattering loss in the laser cavity. The filter is a water proof HEPA (High Efficiency Particulate Air) filter, originally developed for semiconductor factories, designed to stop particles as small as 0.3 μm. The entire system is evacuated and kept at 70 Pa by a rotary pump with a capacity of 3000 l/min. The operation is conducted as follows: first, V2 is kept open, V1 of each SOG is kept closed, and the Cl_2 tank contains 0.1–0.4 MPa of pure chlorine gas. Just before operation, V2 is closed to isolate the cavity from the vacuum system. Immediately after V2 is closed, the two V1s are opened simultaneously, and the Cl_2 gas is injected into the inside of the porous pipe. A blast through its perforated wall causes reaction (1) to occur on its outer surface allowing singlet oxygen to fill the laser cavity. Since V1 is a pneumatic high-speed butterfly valve, its opening time is as short as 50 ms. When the pumping action has ceased, V2 is opened again to evacuate the whole system and to prepare it for the next shot.

We measured the pressure of the laser cavity by a semiconductor pressure sensor (Kopal PA-500-351A), and the $O_2(a^1\Delta_g)$ density by measuring the 1270 nm fluorescence by a filtered Ge photodiode (Hamamatsu B1919). The end light is also detected by another Ge photodiode. Apart from the laser experiments, the losses of the cavity were measured. Figure 7b shows the setup. A HeNe laser beam passes through the optical axis of the cavity, and the beam intensity is monitored at the other side of the cavity. When the system is operated, the intensity of the detected light changes due to scattering or absorption losses. The change in beam intensity indicates the time history of the cavity losses per pass.

Care was taken to ensure that the optical losses are kept as minimal as possible. The losses, apart from the mirror losses, are mainly due to two causes: one is diffraction in the resonator and the other is the operation of the SOG. For the former cause, the diffraction losses are negligible in our situation since the Fresnel number of the resonator is chosen such that a few transverse modes of low order are allowed to oscillate. For the TEM_{11}-mode, e.g., with mirror spot sizes of about 2 and 2.4 mm the loss per pass is below 0.01%. For the latter cause, losses may originate from the deposition of aerosols on the mirrors and the hydrodynamic motion of the laser medium. We operated the SOG using nitrogen gas instead of chlorine, to find out how large the losses caused by these processes may be. The experimental setup was the same as Fig. 7b. The observed change in intensity of the HeNe laser was lower than the resolution limit of the digital oscilloscope (0.5%). In addition, the resonator mirrors were cleaned before each operation to make the mirror losses as minimal as possible. We therefore believe that the round-trip loss of the resonator is the same as the nominal value.

4 Results and Discussion

4.1 Quenching of $O_2(a^1\Delta_g)$ *at the* HEPA *Filter*

As noted in the preceding section, we used a HEPA filter in the SOG. Its effect on the performance of the SOG

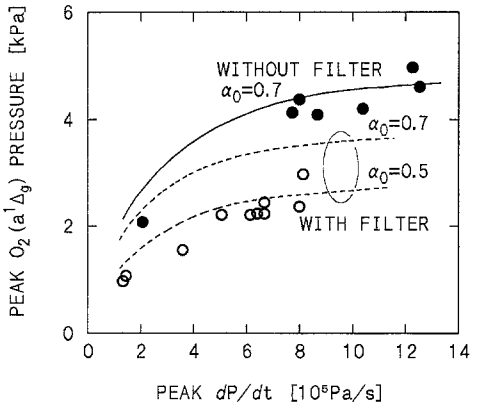

Fig. 8. Observed peak $O_2(a^1\Delta_g)$ pressure as a function of peak (dP/dt). Top trace: Model calculation result of the without-filter system. Middle and bottom traces: Model calculation results of the with-filter system

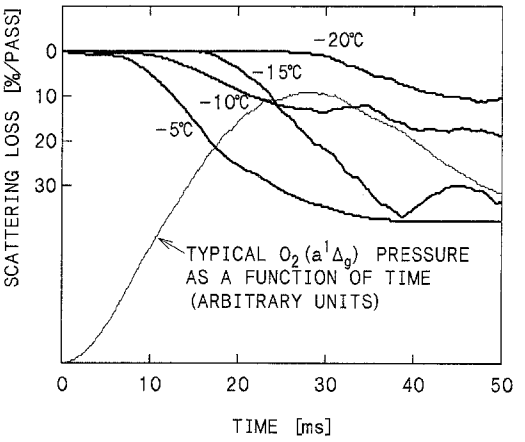

Fig. 9. Scattering loss of the cavity as a function of time at various solution temperatures. Pressure of the Cl_2 tank was 0.35 MPa

was examined for the first time. We compared the observd results to the model calculations in order to estimate the $O_2(a^1\Delta_g)$ loss caused by the HEPA filter unit. Figure 8 shows the peak $O_2(a^1\Delta_g)$ pressure as a function of the peak pressure-increase rate (dP/dt). The solid dots show the results observed when the system was operated without the HEPA filter, while the open dots represent the results with the HEPA filter. Three lines represent the results of model calculations conducted under different boundary conditions. The top solid line represents the result in which the boundary conditions are equal to the solid dots, and the middle dashed line shows the predicted $O_2(a^1\Delta_g)$ peak of the system when the HEPA filter was attached. Although the deactivation caused by the HEPA filter is not considerd in our model, the calculated peak $O_2(a^1\Delta_g)$ pressure of the with-filter system is lower than that of the without-filter system since the volume of the system increased significantly because of the use of the HEPA filter. However, the observed results were still lower than the values predicted by the middle line. The bottom curve represents calculated results under the same boundary conditions as those used for the middle curve, except that the initial yield of the SOG (α_0) was lowered from 0.7 to 0.5. The observed results neatly fit this curve. It means that about 30% of $O_2(a^1\Delta_g)$ molecules are deactivated while passing through the filter. As a consequence, the effective yield of the SOG decreased from 0.7 to 0.5.

4.2 Scattering Losses

The scattering losses of the cavity were measured as a function of time at various solution temperatures. Figure 9 shows the results along with a typical time history of the $O_2(a^1\Delta_g)$ pressure. It is shown that the scattering losses strongly depend on the solution temperature. In fact, no oscillations are expected at temperatures of $-10°$ C or higher. On the other hand, as we stated in the previous section, the measured losses were always within the resolution of the measurement system when the system was operated with the N_2 gas. This result indicates two facts. One is that the splashes produced in the SOG were completely blocked by the HEPA filter, and the other is that the scattering losses in the cavity are mainly related to reaction (1). This leads to the conclusion that the scattering losses were caused by aerosols formed in the laser cavity by the condensation of water vapor after passing through the HEPA filter. The report of Zagidullin et al. [18], which states that the produced water-vapor concentration is 2.7 times higher than that of the oxygen, supports this interpretation. Although we can avoid scattering losses by cooling the solution to $-20°$ C, the device does not work properly under those conditions. In the next paragraph, the effect of the solution temperature on the $O_2(a^1\Delta_g)$ pressure obtained is discussed.

4.3 $O_2(a^1\Delta_g)$ Pressure as a Function of the Solution Temperature

Figure 10 shows the peak $O_2(a^1\Delta_g)$ pressure as a function of the solution temperature. The $O_2(a^1\Delta_g)$ pressure decreased abruptly when the solution was cooled to $-20°$ C. This result contradicts our cw COIL experiments with a porous-pipe type SOG, where the temperature of the working solution was cooled to $-30°$ C [5]. The probable reason is that for the pulsed regime, the reaction rate of (1) measured per unit surface of the gas-liquid interface per unit time is a few orders of magnitude higher than that observed for continuous operation. Therefore, the effect of the degradation of the reaction rate with temperature is more severe than in the low-pressure continuous operation.

In conclusion, we could neither operate the pulsed SOG at a high solution temperature nor at a low solution temperature under the present circumstances. In addition, there were significant $O_2(a^1\Delta_g)$ losses in the HEPA filter. Therefore, we have not yet observed any laser oscillations.

Presently, we are considering two methods to reduce the losses caused by the aerosols. One method is to remove the aerosols without controlling the production of the water vapor, and the other method is to control it by cooling the working solution. The first method will be done by introducing condensation chamber between the SOG and the laser cavity. The aerosols may be stopped after they have been forced to condense in the condensation chamber. However, this method does not help to overcome the problem of $O_2(a^1\Delta_g)$ quenching in the HEPA filter. We must solve this

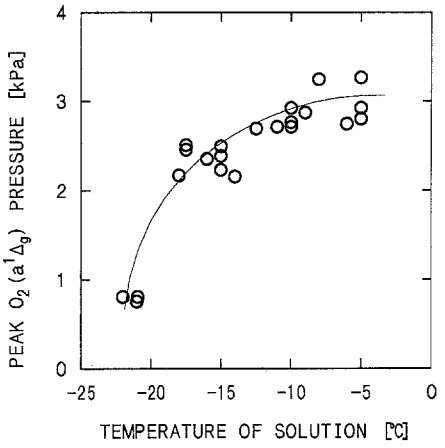

Fig. 10. Peak $O_2(a^1\Delta_g)$ pressure as a function of the solution temperature

difficulty by cooperation with the manufacturer of the air filters.

The second method will be more effective and realistic. We already found that the scattering losses became negligible when the working solution was cooled to $-20°$ C. At this temperature the HEPA filter may not be necessary any more because most of the aerosols will be trapped by the pre-filter, which is located between the HEPA filter and the SOG. The problem is the poor $O_2(a^1\Delta_g)$ yield at lower temperatures. We are planning to test a variety of porous pipes of different materials, thicknesses, and average pore sizes, and we will vary the composition of the working solution. Zagidullin et al. [13] reported that the key to an increase of the yield under the pulsed reaction regime is the specific phase contact area, which is closely related to the characteristics of the porous pipe in our SOG. Further improvements of the SOG are aimed at a higher $O_2(a^1\Delta_g)$ yield with a synchronous lower production of water vapor.

4.4 High-Power and Short-Pulse Operation

Finally, we will discuss briefly the high-power and short-pulse operation of an $O_2(a–X)$ laser. Generally, the internal intensity of the cavity would be quite high when lasing is achieved. In our calculations, the predicted internal intensity is 24 MW/cm^2 at a small-signal gain coefficient of 10^{-5} cm^{-1}. This is still lower than typical damage thresholds of optical components. However, normal resonators cannot be used at high-power, short-pulse operation. The energy extraction will thus be done using a master-oscillator power-amplifier scheme employing the multipass amplifier technique or other methods. This subject has been discussed by Kerber et al. [3].

5 Conclusion

A theoretical and experimental study of a chemically pumped singlet oxygen molecule laser was conducted. A numerical model based on a previously reported high-pressure pulsed singlet oxygen generator was developed, then the population inversion and the small-signal gain of a proposed $O_2(a–X)$ laser were estimated. The calculation showed that a small signal gain of 3×10^{-6}cm^{-1} ought to be obtained by our apparatus. Therefore, lasing should be possible if there were no extra losses other than the losses due to the resonator mirrors. It was pointed out that it should suffice to improve the initial yield of the SOG in order to achieve lasing. A specific energy of 70 J/l and a chemical efficiency of 3.7% is expected for our device if the small-signal gain can be managed to raise to 10^{-5}cm^{-1}.

In accordance with the theoretical calculations, a laboratory device was constructed. A high-efficiency particulate air filter (HEPA filter) was used to minimize the scattering losses caused by the water splashes produced in the singlet oxygen generator. The $O_2(a^1\Delta_g)$ quenching by the HEPA filter was measured for the first time, which turned out to be 30% of the passed oxygen. While the blocking effect of the filter was perfect, there were still significant scattering losses. These losses were probably caused by the aerosols produced by the water vapor condensing in the laser cavity. As a result, we have not yet obtained any laser oscillations. Finally, we point out that an improvement of the air filter and the water-vapor control are the keys realizing the $O_2(a–X)$ laser.

Acknowledgements. We wish to acknowledge productive interactions with Soichiro Ikeda of the Oshitari Laboratory Co. Inc., and we also acknowledge Dr. Sanichiro Yoshida for critical reading of the manuscript and for many helpful discussions.

References

1. R.M. Badger, A.C. Wright, R.F. Whitlock: J. Chem. Phys. **43**, 4345–4350 (1965)
2. M.O. Scully, R.F. Shea, K. Kompa: J. Opt. Soc. Am. B **3**, 996–1005 (1986)
3. R.L. Kerber, A.K. MacKnight, R.D. Franklin: Appl. Opt. **17**, 3276–3283 (1978)
4. K. Takehisa, N. Shimizu, T. Uchiyama: J. Appl. Phys. **61**, 68–73 (1987)
5. T. Kikuchi, T. Tsuruyama, T. Uchiyama: J. Appl. Phys. **64**, 2873–2878 (1988)
6. M. Endo, K. Kodama, Y. Handa, T. Uchiyama: J. Appl. Phys. **71**, 5760–5767 (1992)
7. G.M. Barrow: *Introduction to Molecular Spectroscopy* (McGraw-Hill, New York 1962) pp. 98–103
8. F.D. Findlay: Can. J. Phys. **47**, 687–691 (1969)
9. L. Herzberg, G. Herzberg: Astrophys. J. **105**, 353–359 (1947)
10. J.H. Miller, R.W. Boese, L.P. Giver: J. Quant. Spectrosc. Rad. Transfer **9**, 1507–1517 (1969)
11. J.H. Van Vleck: Astrophys. J. **80**, 161–170 (1934)
12. I. Kovács: *Rotational Structure in the Spectra of Diatomic Molecules* (Hilger, London 1969) pp. 175–182
13. M.V. Zagidullin, A.Yu. Kurov, N.L. Kupriyanov, V.D. Nikolaev, M.I. Svistun, N.V. Erasov: Sov. J. Quant. Electron. **21**, 747–753 (1991)
14. R.J. Richardson, J.D. Kelly, C.E. Wiswall: J. Appl. Phys. **52**, 1066–1071 (1981)
15. O. Aharon, A. Elior, M. Herskowitz, E. Lebiush, S. Rosenwaks: J. Appl. Phys. **70**, 5211–5220 (1991)
16. A.I. Ddyukov, Yu.A. Kulagin, L.A. Shelepin, V.N. Yarygina: Sov. J. Quant. Electron. **19**, 578–587 (1989)
17. P. Borell, H. Rich: Chem. Phys. Lett. **99**, 144–147 (1983)
18. M.V. Zagidullin, V.I. Igoshin, V.A. Katulin, N.L. Kupriyanov, N.N. Yuryshev: Sov. J. Quant. Electron. **14**, 139–140 (1984)